Korean J. Chem. Eng., 32(11), 2187-2203 (2015)
DOI: 10.1007/s11814-015-0032-z

pISSN: 0256-1115
eISSN: 1975-7220

Flow and heat transfer characteristics in a channel having furrowed wall based on sinusoidal wave

Jiansheng Wang†, Xiaoming Gao, and Weiyi Li

Key Laboratory of Efficient Utilization of Low and Medium Grade Energy, MOE, Tianjin University, Tianjin 300072, China
(*Received 17 October 2013 • accepted 9 February 2015*)

Abstract−The effect of wall geometry on the flow and heat transfer in a channel with one lower furrowed and an upper flat wall kept at a uniform temperature is investigated by large eddy simulation. Three channels, one with sinusoidal wavy surface having the ratio (amplitude to wavelength) α/λ=0.05 and the other two with furrowed surface derived from the sinusoidal curve, are considered. The numerical results show that the streamwise vortices center is located near the lower wall and vary along the streamwise on various furrow surfaces. The furrow geometry increases the pressure drag and decreases the friction drag of the furrowed surface compared with that of the smooth surface; consequently, the total drag is increased for the augment of pressure drag. As expected, the heat transfer performance has been improved. Finally, a thermal performance factor is defined to evaluate the performance of the furrowed wall.

Keywords: Channel Flow, Furrowed Surface, Recirculation Zone, Heat Transfer

INTRODUCTION

Energy crisis and sustainable development demand have been driving research efforts towards more energy efficient equipment and processes. To find efficient heat transfer surfaces without a substantial drag increment is a key to improve the thermal performance and increase the compactness of a heat exchanger.

It is well known that heat transfer enhancement can be achieved by various surface geometries, including structured wall furrow [1]. Many investigations have indicated that the modified geometrical surface can strengthen the disturbance in boundary layer. Sawyers et al. [2] numerically studied the effect of three-dimensional laminar flow hydrodynamics characteristics on the steady-state heat transfer enhancement of corrugated channels. Naphon [3] investigated the heat transfer performance and pressure drop of the channel with V corrugated upper and lower plates. As a typical surface used for heat transfer enhancement, the wavy surface has been paid more attention [4,5].

The flow in wavy channels was first analyzed by Burns and Parks [6]. Goldstein and Sparrow [7] first used naphthalene to measure local and average heat transfer coefficients in a corrugated wall channel and reported the existence of longitudinal vortices. Zilker et al. [8,9] presented the measurement of the pressure and shear stress of the wavy surface. Kruse and von Rohr [10] studied the turbulent heat flux at a heated sinusoidal wavy wall using a particle image thermometry technique. They found that larger scale structures made a significant contribution to the streamwise heat flux, and smaller scales were more important to the wall-normal heat flux. Kuhn and von Rohr [11] studied the mixed convection of a heated wavy surface. They revealed that two dominant scalar structures induced by buoyancy effects and the local wall curvature had the most influence on vertical transport.

Maaβ and Schumann [12] found that the effective friction velocity at wavy wall increased by about 50% compared with that at the flat wall due to the additional pressure drag. Choi and Suzuki [13] found that the separated shear layer and the near-wall streamwise vortices played an important role for the heat and momentum transfer near the wavy wall. Kuhn et al. [14] numerically investigated mixed convective flow over a heated wavy surface and obtained significant heat transfer enhancement. Wang and Chen [15] numerically analyzed the heat transfer of a sinusoidal surface. The results showed that the lowest skin-friction coefficient and Nusselt number occurred upstream within a short distance of the maximum section of each wave. Park et al. [16] found that the Nusselt number distribution was periodical in the streamwise of the wavy surface. Park et al. [17] slightly modified the nonlinear model of Park et al. [16] and found that the drag and heat transfer coefficient of the wavy surface were higher than that of the flat surface, which related to the appearance of the flow recirculation zone. Dellil et al's [18] results showed that the minimum and the maximum Nusselt numbers at wavy surface appeared near to the separation and the reattachment points, respectively, and the averaged Nusselt number was enhanced with the increase of the wave amplitude, accompanied by the augment of the pressure drop. Yoon et al. [19] numerically investigated the effect of wave amplitude on turbulent flow in a wavy channel. The small scale recirculating flow near the trough and the mean reverse flow were observed. Naphon [20] found that the sharp edge of wavy plate has a significant effect on the flow structure and heat transfer enhancement. Hafez et al. [21] investigated turbulent flow over a sinusoidal solid surface using two versions of standard k-ε turbulence model. Barboy et al. [22] investigated the fluid flow and heat transfer in a channel with a wavy wall heated by constant heat flux. The highest temperature occurred in the position down the crest, and the position with lowest temperature was

†To whom correspondence should be addressed.
E-mail: jsw@tju.edu.cn

adjacent to reattachment point.

As mentioned above, a number of investigations on the flow and heat transfer characteristics of wavy or relevant surface have been performed. Most works focus on the heat transfer enhancement and the suppression on the increase of flow drag is neglected on some extent. In addition, the synthetic evaluation on the heat transfer performance is usually ignored, more or less. In fact, a higher flow resistance may restrict the application of wavy surface in engineering field in despite of having efficient heat transfer performance. Simple improvement of heat transfer performance with wavy surface may lead to energy wasting derived from the increase of flow resistance. Previous results indicate that the heat transfer and flow characteristics in peak and trough, upslope and downslope regions of the wavy surface have distinct features. So, based on the available results of wavy surface, modifying the wavy surface appropriately is necessary for obtaining efficient heat transfer performance and lower flow resistance.

We did a numerical investigation of turbulent flow and heat transfer in a channel with one furrowed lower wall and a plate top wall using large eddy simulation. The aim of the present work is to explore the flow and heat transfer characteristics in channels with various wavy geometry configurations. It has been found that the flow structure at different region of the wavy surface has a distinct influence on fluid flow and heat transfer characteristics. So, it is predicted to probe a wavy geometry surface with relative efficient heat transfer performance and lower flow resistance. To seek the surface with lower flow drag, three types of furrowed bottom walls, one a sinusoidal wavy wall and the other two furrowed walls derived from the sinusoidal wavy wall are applied. From the view of practical engineering application, the considered wavy surfaces have more possibility of being applied in thermal equipment such as a heat exchanger. The sinusoidal wavy wall is selected for the purpose of probing the influence of geometric parameter, such as length of plateau on the features of flow and heat transfer. The present modified wavy surfaces are selected for suppressing the increase of flow resistance and being applied easily in practical engineering, such as a heat exchanger. Moreover, we focus on providing quantitative information about the flow and heat transfer features, such as the distributions of velocity, temperature, turbulence intensities, heat flux, drag coefficient and Nusselt number of various furrowed surfaces.

PROBLEM DESCRIPTION

The present work is concerned with the unsteady turbulent flow in a three-dimensional furrowed channel with the upper flat and a lower furrowed wall. The upper and the lower wall are kept at uniform temperature. According to the minimum channel size of turbulent flow proposed by Jimenez and Moin [23], the computational domain is set up with the reference of works by Kim et al. [24] and Maaβ and Schumann [12]. The periodic boundary in streamwise can insure the turbulence of channel in full developed state with limited computational domain, and the periodic boundary in spanwise can insure the channel walls in spanwise has little influence on the statistic properties of turbulence. In the present work, a numerical simulation is conducted about 80 periodic times in streamwise of the channel, and the statistic properties of turbulence in channel are steady. In this situation, the turbulence in the channel can be considered to be fully developed turbulence. The computational domain is shown in Fig. 1(a), which has dimensions of $4\lambda\times\lambda\times2\lambda$ in the streamwise, wall-normal and spanwise direction.

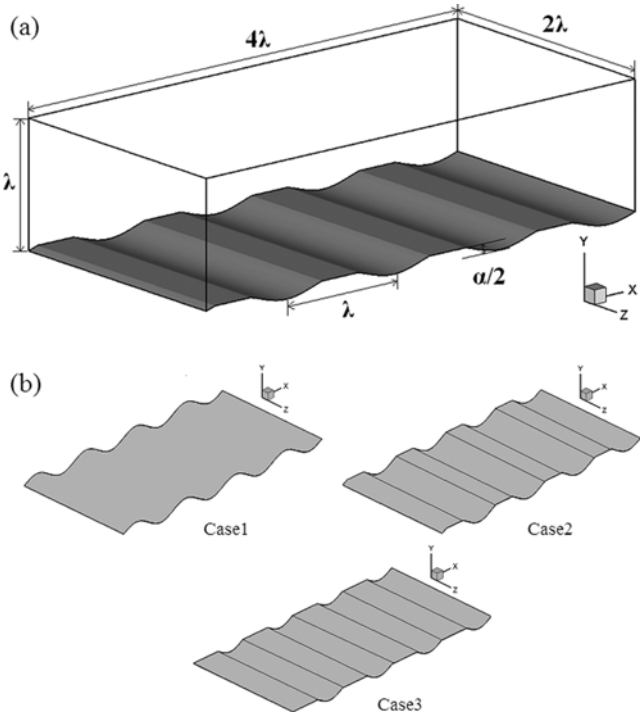

Fig. 1. Schematic diagram of the physical model: (a) Computational domain, (b) present three cases.

Computation has been performed for three cases with different furrowed bottom wall when $Re_b=(U_b\cdot\delta)/v=2800$, where v denotes the kinematic viscosity, δ represents the half-height of the channel, and U_b is the bulk velocity. The main geometry difference among the three cases is the shape of the lower wall. In case 1, the bottom is a conventional wavy wall characterized by the ratio of amplitude to wavelength $\alpha/\lambda=0.05$. The wavelength λ is equal to the channel height H. The profile of the lower wall is represented by $y_w=\alpha\sin(2\pi x/\lambda)$, with the mean position located at y=0. The upper flat wall of the channel is located at y=H. In case 2, the lower wall is formed by cutting the sinusoidal wavy wall of case 1 with a x-z plane at y_h, where y_h is the distance from the plane at y=0 to the cutting x-z plane in the wall-normal direction. We consider $y_h=\alpha/2$ in case 2 and $y_h=0$ in case 3. Three cases employed in present work are shown in Fig. 1(b).

MATHEMATICAL FORMULATION AND NUMERICAL METHOD

1. Governing Equations

We assumed the flow to be unsteady, three-dimensional, incompressible turbulent. The equations describing turbulent flow and heat transfer are given by the conservation of mass, momentum and energy. In large eddy simulation, filtered forms of the continuity and momentum equations for incompressible fluid are expressed as follows:

$$\frac{\partial \overline{u}_i}{\partial x_i} = 0 \tag{1}$$

$$\frac{\partial \overline{u}_i}{\partial t} + \frac{\partial (\overline{u}_i \overline{u}_j)}{\partial x_j} = -\frac{1}{\rho}\frac{\partial \overline{p}}{\partial x_i} + \nu \frac{\partial^2 \overline{u}_i}{\partial x_j \partial x_j} - \frac{\partial \overline{\tau}_{ij}}{\partial x_j} \tag{2}$$

where $\overline{u}_i$, $\overline{p}$ and $\overline{\tau}_{ij}$ are filtered velocity, filtered pressure and subgrid-scale stress tensor, respectively, the indices i, j refer to the directions of coordinates. The subgrid-scale stress tensor is defined as $\overline{\tau}_{ij} = \overline{u_i u_j} - \overline{u}_i \overline{u}_j$.

The large eddy simulations are performed by using the Smagorinsky-Lilly model [25] for the subgrid scales,

$$\tau_{ij} - \frac{1}{3}\tau_{kk}\delta_{ij} = -2\mu_t \overline{S}_{ij} \tag{3}$$

The eddy viscosity is defined as

$$\mu_t = (C_s \Delta)^2 |\overline{S}| \tag{4}$$

where C_s is Smagorinsky coefficient, and Δ denotes the length scale of the unresolved motion obtained from the volume of the computational cell ΔV,

$$\Delta = (\Delta V)^{1/3} \tag{5}$$

and $|\overline{S}|$ is the magnitude of the strain rate given in the following equation:

$$|\overline{S}| = \sqrt{2\overline{S}_{ij}\overline{S}_{ij}} \tag{6}$$

$$\overline{S}_{ij} = \frac{1}{2}\left(\frac{\partial \overline{u}_i}{\partial x_j} + \frac{\partial \overline{u}_j}{\partial x_i}\right) \tag{7}$$

The filtered form of the energy equation used in the present study is expressed as follows:

$$\frac{\partial \overline{T}}{\partial t} + u_j \frac{\partial \overline{T}}{\partial x_j} = \frac{\nu}{Pr}\frac{\partial^2 \overline{T}}{\partial x_j \partial x_j} - \frac{\partial \overline{h}_j}{\partial x_j} \tag{8}$$

where $\overline{T}$ is filtered temperature and $\overline{h}_j$ is the subgrid-scale heat flux defined as

$$\overline{h}_j = \overline{u_j T} - \overline{u}_j \overline{T} \tag{9}$$

2. Numerical Details

Normalized temperature $\theta = (T_w - T)/(T_w - T_{in})$, where T_{in} denotes the inlet temperature of fluid, while T_w is the wall temperature. The Prandtl number is set as Pr=0.71 with the reference of work by Kadar [27]. Meantime, the Prandtl number of air is near 0.71. So, Pr=0.71 has more practical significance for engineering application. Where $Pr = \upsilon/a$, υ (m^2/s) and a (m^2/s) is the kinematic viscosity and thermal diffusivity of fluid, respectively. No-slip conditions are applied to both the upper and lower wall, and spatially periodic boundary conditions are assigned in the spanwise and streamwise directions. The upper and the lower wall are kept at a uniform temperature. All above-mentioned equations accompanied by boundary conditions are solved using finite volume method. The well-known SIMPLE algorithm [28] is used in the numerical process. The convective and diffusive terms of the discretized equations are approximated by a second-order central difference scheme. The Crank-Nicholson scheme is applied for the discretization of the time term. The value of the time and space interval is selected to ensure that the value of CFL<0.5. The CFL is defined as $CFL = u\Delta\tau/\Delta x$, and Δx are time and space interval, respectively. The higher value of CFL means that the convergence in numerical simulation proceeds faster and the stability becomes worse. In physics, the CFL means the ratio of -marching time in numerical simulation process to the time of the mechanical disturbance propagation. The simplest to understand is: the time-marching speed must be faster than the spread speed of physical disturbance.

Table 1. Grid independence study at Re=2800

Grid sizes (nodes)		Nusselt number Nu	Friction factor C_f
(80×65×40)	208000	8.217	0.00755
(120×65×60)	468000	8.621	0.00791
(120×110×60)	792000	8.811	0.00807
(140×110×80)	1232000	8.981	0.0082
(160×129×80)	1651200	9.064	0.00827
(180×129×90)	2089800	9.081	0.00828

To ensure the accuracy of the numerical results, a check for the grid independence of the numerical solutions is conducted by six different grids for the flat channel. The grid size in the streamwise, spanwise and wall-normal directions along with the obtained Nusselt number $Nu = h\delta/k$ and skin friction coefficient $C_f = 2\tau_w/\rho U_b^2$ are shown in Table 1. Finer grid may give a more accurate solution. However, the improvement of the accuracy of computation will decrease gradually when the number of grid points increases beyond a certain level. As shown in Table 1, a difference in the obtained results is not evident when the node numbers are more than 1651200. Compared with the results of the finest computational domain grid, the relative deviation of the obtained Nusselt number and friction factor of grid 160×129×80 is 0.19% and 0.12%, respectively. To lower computational costs, 160×129×80 is selected as the final grid in the later numerical simulation. Since the furrow surface geometry is easy to represent, hexagonal control volumes are employed. The grid is equidistant in the streamwise and spanwise directions. The grid near the wall in normal is refined using the bell shaped scheme considering the high gradient of the parameters. The bell shaped scheme means that the distribution of grid interval in normal obeys the bell shape function ($\Delta y = e^{-y^2}$, and y=0 is located at the normal center of the channel). In this scheme, the grid interval increases with the augment of normal distance to the wall. The grid near the wall is dense and becomes sparse with the increase of the normal distance to the wall. The y+ values of the first layer grid are less than 0.4; therefore, the boundary layers can be fully resolved. It means that the parameters variation such as temperature and velocity in the high gradient boundary layer can be captured.

RESULTS AND DISCUSSION

1. Validation of the Present LES

The simulation of the turbulent flow and heat transfer in a plane channel is essential to check the accuracy of our approach in per-

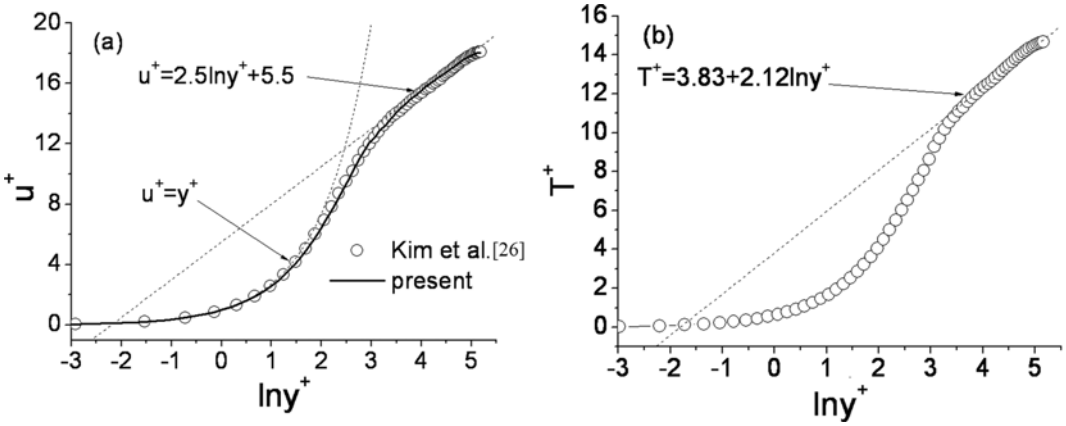

Fig. 2. Mean velocity and temperature profiles: (a) Mean velocity, (b) mean temperature.

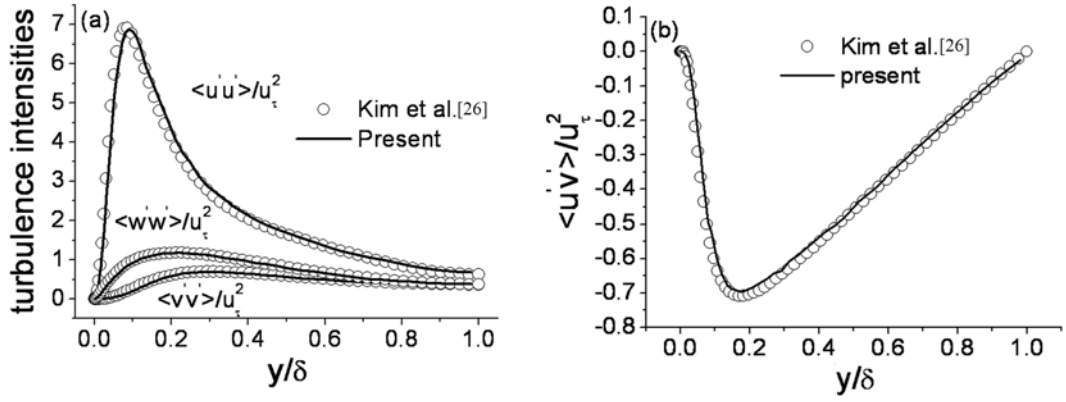

Fig. 3. Comparison with Kim et al. data: (a) Velocity fluctuations, (b) Reynolds shear stress.

forming the LES at a bulk Reynolds number Re_b=2800, which is equivalent to $Re_\tau=u_\tau\delta/\nu$=180. The dimension and grid numbers in the streamwise, wall-normal and spanwise direction of the computational domain are the same as the furrow channel. The friction velocity u_τ is defined as $u_\tau=\sqrt{\tau_w/\rho}$. Fig. 2 shows the distribution of mean velocity and temperature, where $y^+=yu_\tau/\nu$. The mean velocity profile, $u^+=u/u_\tau$, as illustrated in Fig. 2(a), is compared with the law of the wall $u^+=2.5\ln y^++5.5$, and the profile obtained from the DNS result by Kim et al. [24]. It shows excellent matching between the profiles. In Fig. 2(b), the mean temperature profile is divided by the average friction temperature, where $T+=\overline{\Delta T}/T_\tau$, $\overline{\Delta T}$ is the temperature difference between the wall and the fluid. The friction temperature $T_\tau=q_w/(\rho c_p u_\tau)$. The absolute value of the temperature difference between the wall and the fluid is compared with the Kader log-law obtained from experiment for Pr=0.71, and has the form of $T^+=3.83+2.12\ln y^+$ [27]. As shown in figure, present results show good agreement with the empirical law.

Other mean properties such as the skin friction coefficient and bulk mean velocity are also compared with the experimental correlations proposed by Dean [29]. In our study, the bulk Reynolds number based on the full channel height is Re_b=5600. The skin friction coefficient C_f is 8.27×10^{-3}, which is in good agreement with the result obtained from Dean's suggested correlation of $C_f=0.073Re_b^{-0.25}=8.44\times10^{-3}$. The ratio of the mean centerline velocity to the mean bulk velocity, U_c/U_b is 1.16, which shows an excellent agreement with the result obtained from Dean's correlation of $U_c/U_b=1.28Re_b^{-0.0116}=1.16$. The obtained Nusselt number is 9.064, which is in good agreement with the result obtained from Gnielinski's suggested correlation [30] $((f/8)(Re-1000)Pr)/(1+12.7(f/8)^{1/2}(Pr^{2/3}-1))=9.289$, where $f=(0.79\ln Re-1.64)^{-2}$ is the friction factor.

The turbulence intensity profiles, based on the streamwise, spanwise and wall-normal fluctuation velocity, and the DNS result of Kim et al. [24] are shown in Fig. 3(a). The turbulence intensity is in agreement with that of two-walled channel flow. Meanwhile, it's found that present results are well consistent with the DNS results. The profile of the present Reynolds stress is illustrated in Fig. 3(b). The present result is in good agreement with that of DNS.

2. Simulation Results of Furrowed Wall Channel Flows

When a fluid flows past a furrowed surface, the flow features such as the alternating occurrence of favorable and adverse pressure gradients, the periodic changes of streamline curvature induced by turbulence structures derived from wall-curvature are different from the counterparts over a flat surface. When the fluid moves downstream from the convergent part into the divergent part of a furrowed wall, the adverse pressure gradient causes the flow near the wall to decelerate until some backflow occurs. Consequently, a flow separation bubble appears near the trough and a separated shear layer forms slightly above the separation bubble. A massive

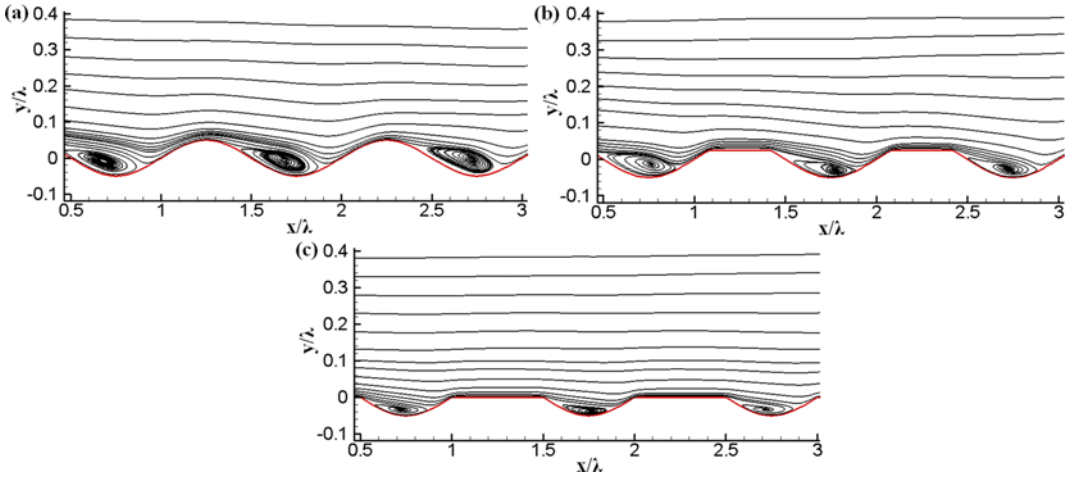

Fig. 4. Mean streamlines of the flow over furrowed walls: (a) Case 1, (b) case 2, (c) case 3.

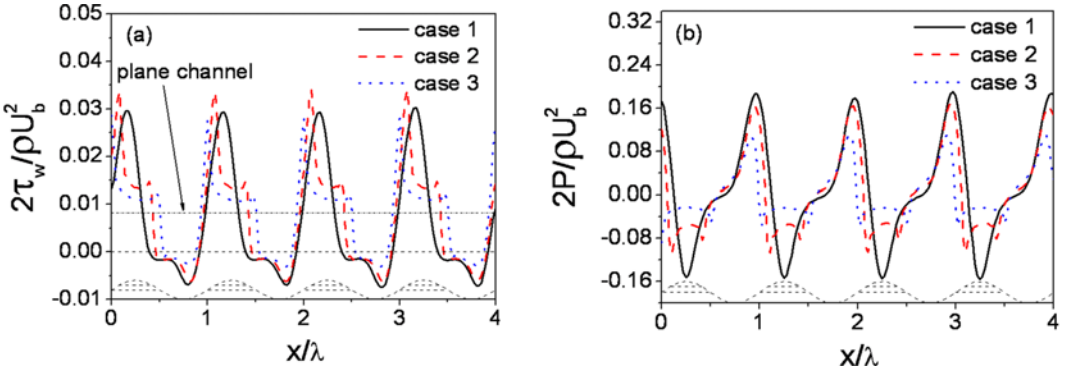

Fig. 5. Distributions of mean friction drag coefficient and pressure drag coefficient along the streamwise direction with varying bottom wall: (a) Friction drag coefficient, (b) pressure drag coefficient.

reversed flow accompanied with some high momentum fluid elements locally penetrate into the separated zone, which promotes the macroscopic mixings between the near-wall and core region fluids. The heat transfer characteristics of flow through such furrowed channels are much more complex than that through parallel plate channels. The boundary layer formed on a furrowed wall is periodically destabilized by flow recirculation, successive acceleration and deceleration associated with multiple flow separations and reattachments which replenish the near-wall fluids with the core region fluids, which results in the augmenting of heat transfer.

2-1. Global Flow and Heat Transfer Characteristics

One of the important features of mean flow in the furrowed channel is the recirculation zone bounded by the separation and reattachment points. Mean streamlines in the x-y plane (perpendicularly to spanwise) for the three types of furrowed wall channels are displayed in Fig. 4. For these cases, the portions from x/λ=0.5 to 3, including three troughs, are shown. For fluid flowing past the furrowed surface, large cells corresponding to the recirculation zones appear in the vicinity of the lower wall and streamlines beyond the troughs are nearly parallel except near the lower wall. Note that the streamlines downstream of the reattachment point are compressed upwards in response to the lifting surface, indicating a significantly accelerated flow. Meantime, the recirculation cell increases in size and its center moves upstream when y_h increases. The flow feature in case 1 is similar to the previous results of wavy surface. When the crest of the wavy surface is removed, the recirculation zone is stretched streamwise for the extrusion derived from main flow in channel. Compared to the previous relevant investigation on wavy surface, the effect scope of recirculation on up-slope and down-slope region of the wavy surface in case 2 and case 3 is close to each other.

The mean friction and pressure drag coefficients distributions along the lower wall of the three cases are plotted in Figs. 5(a) and 5(b), respectively. The pressure drag coefficient, C_p, is defined as $C_p=2p/\rho U_b^2$. In case 1, the friction and pressure drag coefficients present periodic distribution in the streamwise. The friction drag coefficient is least in the trough, increases sharply with a maximum value at the upslope of the wavy surface, and then decreases.

As shown in Fig. 4, the region near the trough is a recirculation zone where the fluid accumulation occurs and the velocity gradient becomes least. The recirculation and accumulation of the fluid pay a critical role in the reduction of the friction coefficient. In the upslope region near the peak of the wavy surface, the velocity increases is derived from mass supplement for the accumulation in the trough region. So, the friction coefficient increases along the upslope of the wavy surface. There is an interesting phenomenon in that the maxi-

mum friction coefficient does not occur at the peak of the wavy surface. The reason is that the velocity near the peak begins to reduce gradually for the effect of the next recirculation and accumulation in downstream. In downslope region, the fluid velocity becomes low for the existence of the recirculation zone. Consequently, the friction coefficient at downslope region reduces gradually. It is obvious that the recirculation caused by wavy surface leads the variation of the friction coefficient.

The variation of friction drag coefficient reflects the alternating appearance of the favorable and adverse pressure gradients or the appearance of flow separations and reattachments induced by the furrows. The pressure drag coefficient also shows an undulated feature with an increase on the upslope side and becomes least near the crest point. Note that the reverse flow causes the distribution of the friction and pressure drag coefficients to deviate from the sinusoidal pattern of the wavy surface in the trough. In cases 2 and 3, the distributions of friction and pressure drag coefficient are similar to that in case 1. The main difference is on the plateau portions where corresponding to the crest in case 1. The friction drag coefficient reaches a peak at the front edge of the plateau and then drops sharply. Then, the friction drag coefficient increases generally and reaches a peak again at the rear edge of the plateau. The

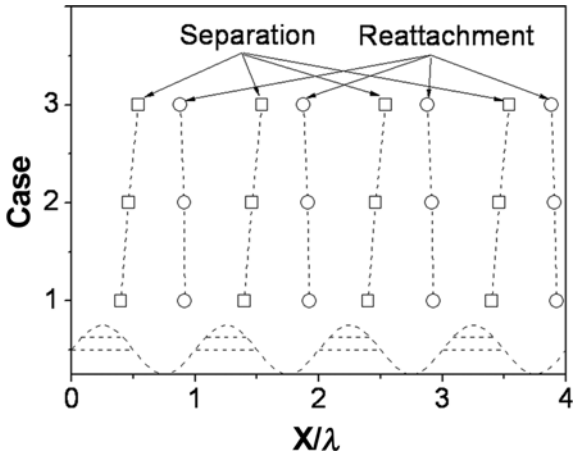

Fig. 6. Locations of separation and reattachment points for three cases.

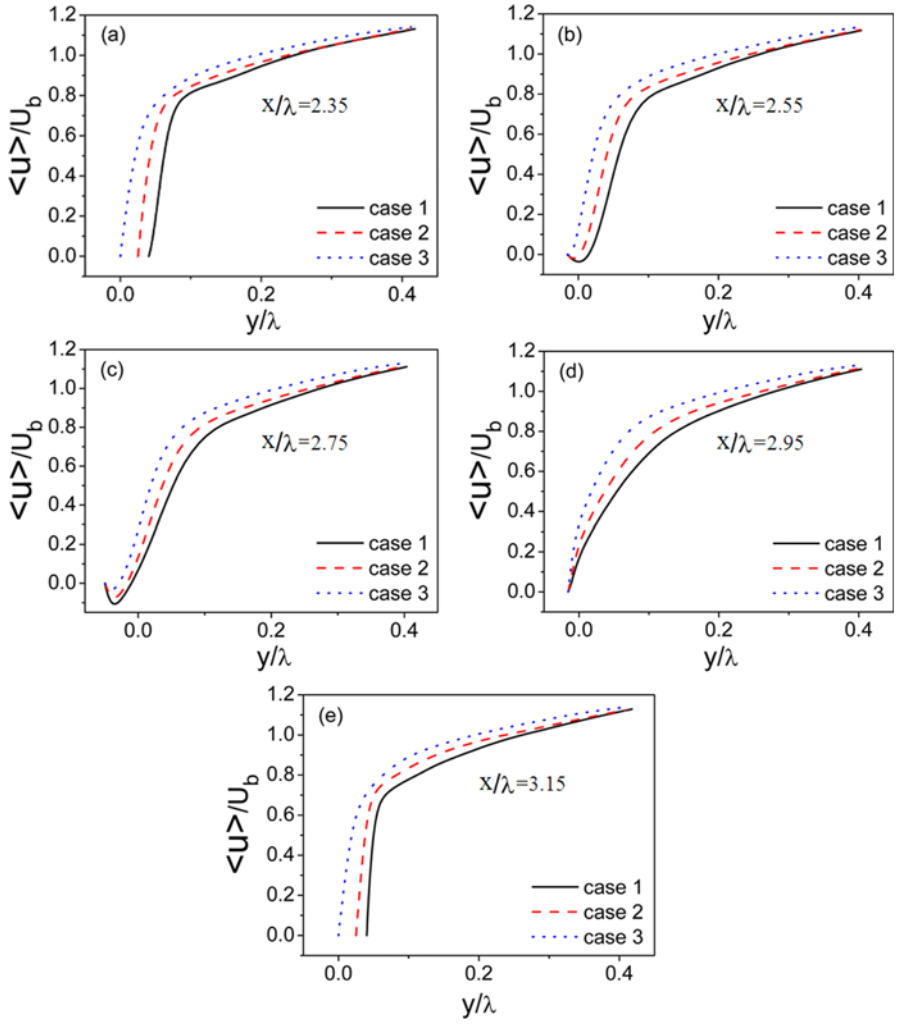

Fig. 7. Profiles of the mean streamwise velocity distributions in the wall-normal direction at different streamwise locations: (a) x/λ=2.35, (b) x/λ=2.55, (c) x/λ=2.75, (d) x/λ=2.95, (e) x/λ=3.15.

peaks of friction drag coefficients at two edges of the plateau are derived from the effect of recirculation flow. At the front edge of the plateau, the fluid is accelerated. Conversely, the fluid is decelerated for the existence of recirculation zone. The recirculation zone at the trough leads to the peak difference of friction drag between the front and rear edge. The pressure drag coefficient reaches a peak at the upslope side of the wavy wall and decreases rapidly to least at the front edge of the plateau. At the plateau, the pressure drag coefficient increases reaches a peak near the middle position, decreases to least at the rear edge of the plateau. Then, it increases gradually until reaching the maximum value at the windward side. The feature of pressure drag coefficient is related to the velocity along the wavy surface. The friction drag coefficient feature embodies the velocity variation. Because the opposite variation trend of the velocity and pressure, it is not difficult to understand that the distribution of pressure drag coefficient is opposite to that of friction drag coefficient. Compared to the results of flat plate as shown in Fig. 5(a), the friction drag coefficient reduces at the trough and increases at the crest (or plateau). The reduction of friction drag coefficient is derived from the accumulation of fluid and the recirculation zone in the trough region. The increase of friction drag coefficient is derived from the separation. The reduction of distance from the position with maximum pressure to that with minimum pressure is caused by the plateau effect in cases 2 and 3, which makes the adverse pressure gradient appearing in case 2 and case 3 to be higher than that in case 1. This results in the friction drag coefficients in cases 2 and 3 being higher than that in case 1 at these positions. The separation and reattachment locations where the friction drag coefficient vanishes are plotted in Fig. 6. The separation and reattachment occur in region having an unfavorable pressure gradient and just upstream of the maximum pressure. The distance between the separation and reattachment points enlarges with the increase of y_h, which indicates the augmenting of the flow separation region is derived from the enhancement of the disturbance caused by the protrusion of the lower wall. It is also observed that the separation point is more sensitive to prominency level than that to reattachment point, which induces the perturbation in boundary layer. In case 2 and case 3, the separation is delayed for the presence of plateau and the reattachment point is almost the same as that in case 1. It means the wavy surface with plateau can reduce the distance between the separation and reattachment point.

The variation of the mean streamwise and wall-normal veloc-

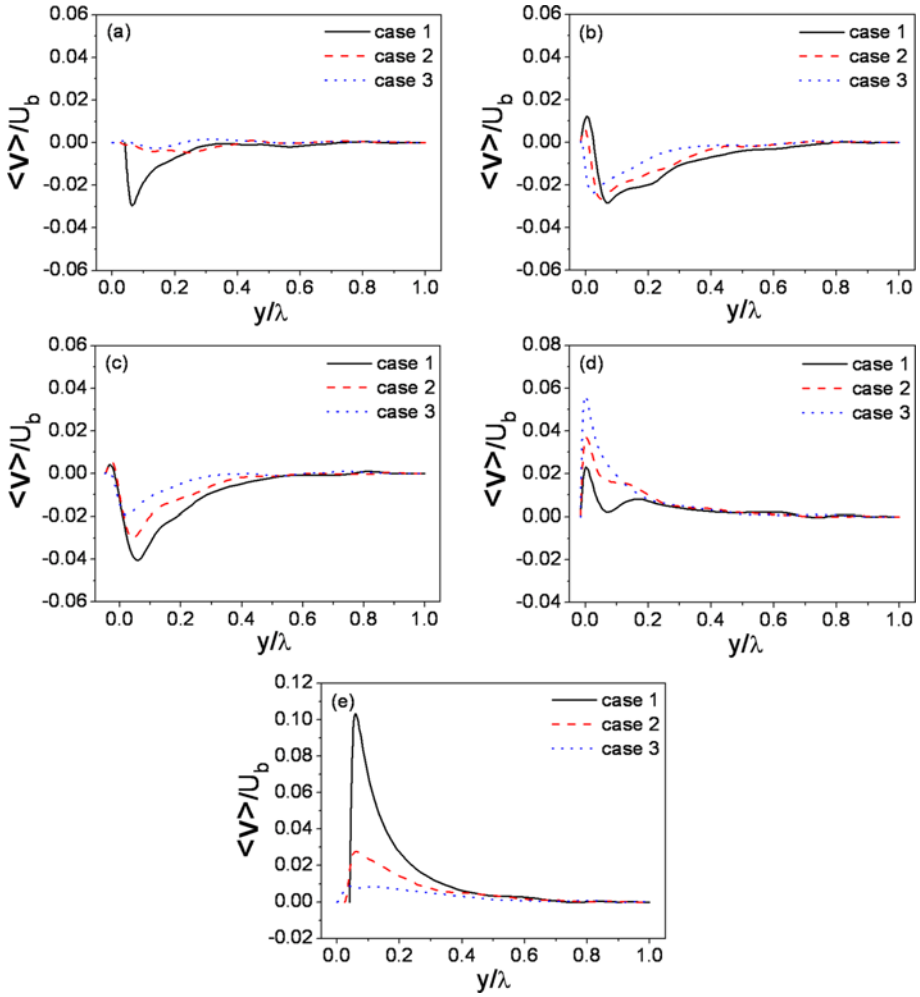

Fig. 8. Profiles of the mean wall-normal velocity distributions in the wall-normal direction at different streamwise locations: (a) x/λ=2.35, (b) x/λ=2.55, (c) x/λ=2.75, (d) x/λ=2.95, (e) x/λ=3.15.

ity along the streamwise plays a vital role in fluid structure near the wall. Fig. 7 and Fig. 8 show the distributions of the streamwise and wall-normal mean velocity, which are obtained at five characteristic streamwise positions (x/λ=2.35, 2.55, 2.75, 2.95, 3.15). In case 1, point a (x/λ=2.35) is located near the crest of the wavy wall and the front of separation point. Points b and c (x/λ=2.55, 2.75, respectively) are located in recirculation region. Points d and e (x/λ=2.95, 3.15, respectively) are located in the rear of reattachment point. Due to the drag at the lower wall is larger than that at the upper flat wall, the streamwise velocity peak is shifted towards the flat top wall and shows the asymmetry. The wall-normal velocity in all cases presents negative values in the separation region, which is derived from the downward motion. The positive values in upslope region close to the lower wall are caused by recirculation.

At x/λ=2.35 just the front of recirculation zone, the mean streamwise velocity, presents positive even near the lower surface as that in flat channel flow, and grows quickly in a short distance. In cases 2 and 3, the wall-normal velocity tends to zero for being located at the plateau and the motion in normal is bounded by the wall. The negative mean wall-normal velocity appears in case 1 for being located at the downslope of the wall.

At x/λ=2.55, 2.75, the mean streamwie velocity presents a negative value due to the effect of the adverse pressure gradient, which indicates the appearance of flow separation and recirculation at the

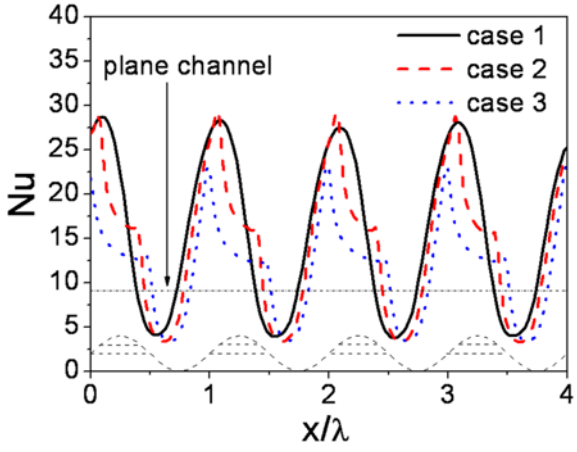

Fig. 9. Mean Nusselt number distributions along bottom wall for different cases.

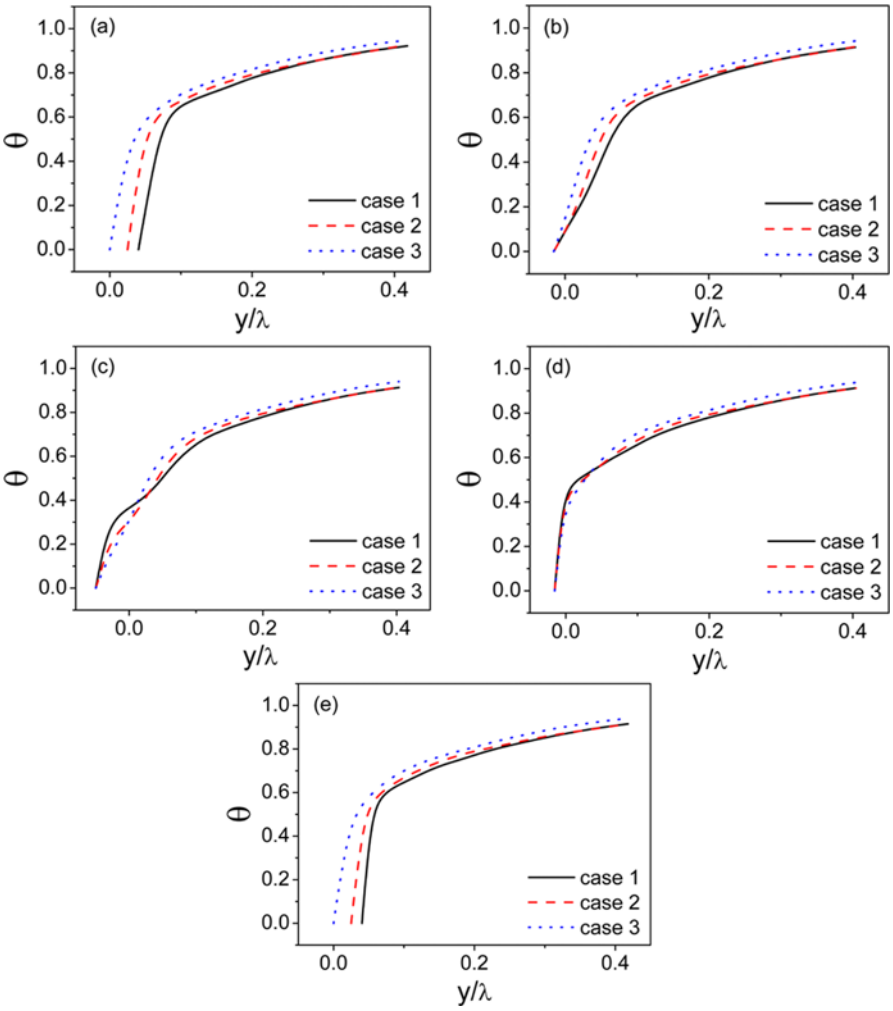

Fig. 10. Mean temperature profiles at different streamwise locations: (a) x/λ=2.35, (b) x/λ=2.55, (c) x/λ=2.75, (d) x/λ=2.95, (e) x/λ=3.15.

downslope side of the wall. The magnitude of velocity in case 1 is larger than that in cases 2 and 3, implying stronger reversed flow occurs. The wall-normal velocity near the lower wall presents the positive values as shown in Figs. 8(b) and Fig. 8(c), which results in the fluid eingb pushed upward along the lower surface by the reversed flow. The magnitude of wall-normal velocity in case 1 is larger than that in cases 2 and 3 for core fluids deep swarm into the trough, which is induced by a stronger reversed flow.

At x/λ=2.95, 3.15 downstream of the reattachment point, the near-wall flow is accelerated by a favorable pressure gradient. The negative streamwise and wall-normal velocity disappear as shown in Figs. 7(d), 7(e), 8(d) and 8(e). At x/λ=2.95, the streamwise velocity gradients in the region close to the walls in cases 2 and 3 are higher than that in case 1. The wall-normal velocity in cases 2 and 3 is larger than that in case 1 on account of the existence of the far upstream reattachment points in cases 2 and 3. At x/λ=3.15, the streamwise velocity gradient in the region close to the wall in case 1 is obviously larger than that in cases 2 and 3, and the wall-normal velocity is larger than that in cases 2 and 3. Above-mentioned flow features indicate that the accelerated region downstream the reattachment point reduces as y_h decreases. Compared with the previous work on wavy surface, it's found that the wall-normal velocity can be affected by the presence of plateau, which has obvious influence on flow and heat transfer characteristics.

As fluid flows over the furrowed heated walls, the breaking and destabilizing thermal boundary layer are promoted by the onset and growth of recirculation zones, resulting in enhancing heat transfer. Fig. 9 shows the variation of the Nusselt number along the lower wall of the channel in three cases. By the way, the smooth parallel-plates case is also plotted for reference purposes as shown in the dash dot black line. Due to the effect of recirculation, at the upstream separation point, hot fluid is pushed away from the heated upper wall, creating a lower heat flux. The cool fluid near the downstream reattachment point is pushed toward the wall, forming a higher heat flux. As a result, the local Nusselt number increases in the converging section and decreases in diverging section accompanied by the minimum and the maximum values near the separation and the reattachment points, respectively. The local Nusselt numbers along the lower wall are larger than that of the plate wall except that at the downslope side of the furrow wall. The minimum Nus-

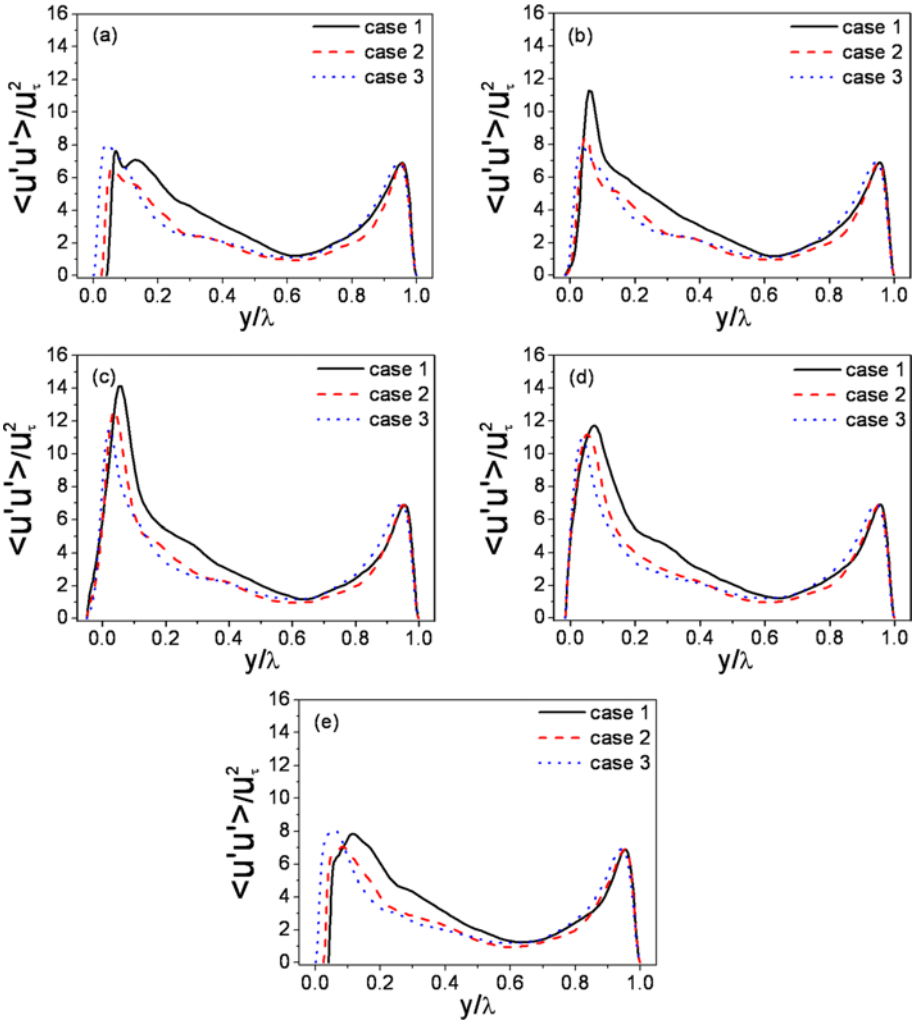

Fig. 11. Mean streamwise turbulence intensities at different streamwise locations: (a) x/λ=2.35, (b) x/λ=2.55, (c) x/λ=2.75, (d) x/λ=2.95, (e) x/λ=3.15.

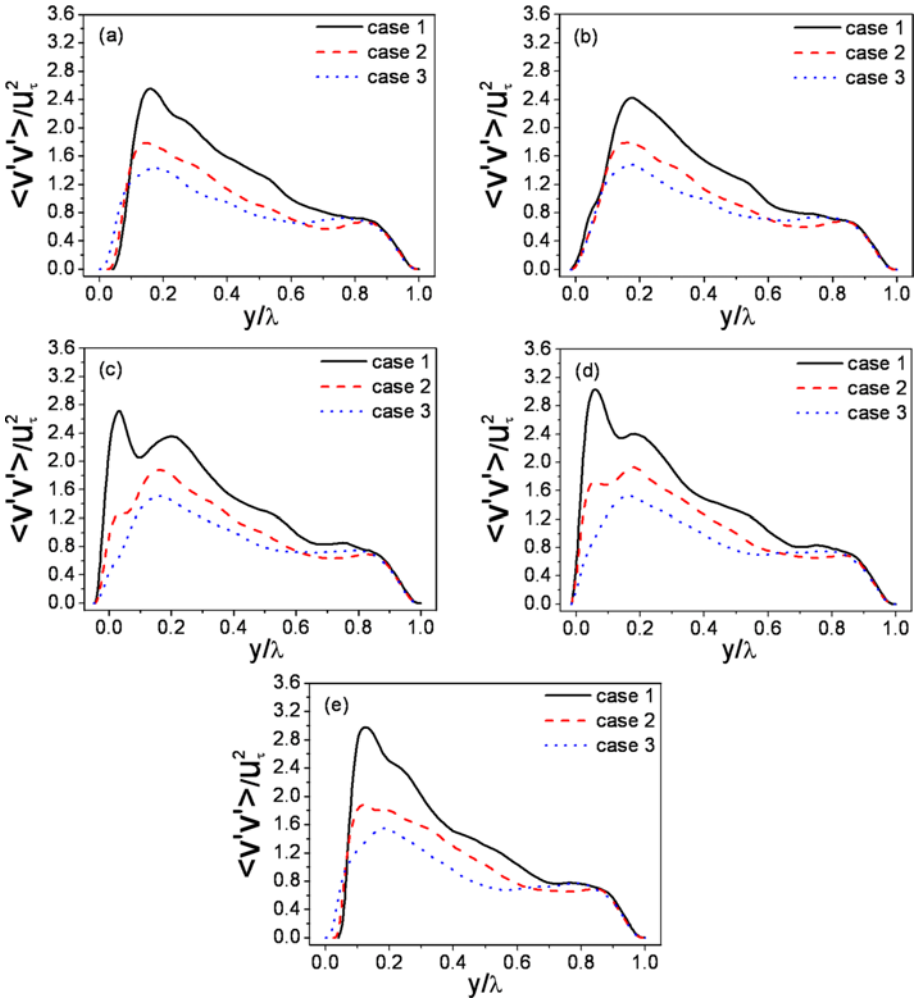

Fig. 12. Mean wall-normal turbulence intensities at different streamwise locations: (a) x/λ=2.35, (b) x/λ=2.55, (c) x/λ=2.75, (d) x/λ=2.95, (e) x/λ=3.15.

selt numbers near the separation points in cases 2 and 3 are smaller than that in case 1 as a result of weaker reversed flow.

The distributions of the mean temperature at five streamwise positions (x/λ=2.35, 2.55, 2.75, 2.95, 3.15) are shown in Fig. 10. The location of maximum temperature is shifted towards the flat top wall due to the furrow effect. At x/λ=2.55, more hot fluids gather near the separation points, leading to a smaller heat flux and a lower temperature gradient in case 1 than that in cases 2 and 3. At x/λ= 2.75, the profile in case 1 has a swell in the region near the lower wall because of the stronger reverse flow. At x/λ=3.15, the temperature gradient is higher because of the presence of higher streamwise velocity gradient and wall-normal velocity.

2-2. Turbulence Intensities and Heat Flux

The turbulence intensity is calculated to provide quantitative information of the velocity field. As fluid flows just downstream of the reattachment point, the accelerated fluid forms an inner boundary layer, which passes over the crest (or plateau), moves away from the lower wall at separation point and then forms a shear layer above the separation cell in which the velocity fluctuations intensity reaches a maximum. The distributions of turbulence intensity in the streamwise and wall-normal directions at five different streamwise locations in three cases are shown in Figs. 11 and 12, respectively. The streamwie turbulence intensity increases rapidly to a maximum value in the proximity of the lower wall and decreases gradually to a minimum. As expected, it reaches a second peak close to the top wall of the channel. The trough between the two peaks shifts upward and the streamwie turbulence intensity near the lower wall is quite large, indicating the effectiveness of furrow on promoting mixing with the outer layer fluid in the channel. At point a, in case 1, two peaks appear for a vortex in spanwise direction formed at the downslope side of the wave, accompanied by more but weaker vortices above it. At points b, c and d, the peak locations of the streamwise turbulence intensity are further away from the lower wall and the values in case 1 are higher than that in cases 2 and 3, indicating shear layer is further away from the wall and stronger mixing induced by penetration of the outer flow spreads deep into the trough. The turbulence intensity in wall-normal reduces with the decrease of the depth of trough. The results are similar to that of Choi's [13].

The peak of turbulence intensity in normal is smaller than that in streamwise. Like the streamwise component, the wall-normal turbulence intensity grows quickly and decreases gradually to a minimum, which is almost the same as another peak in the region close

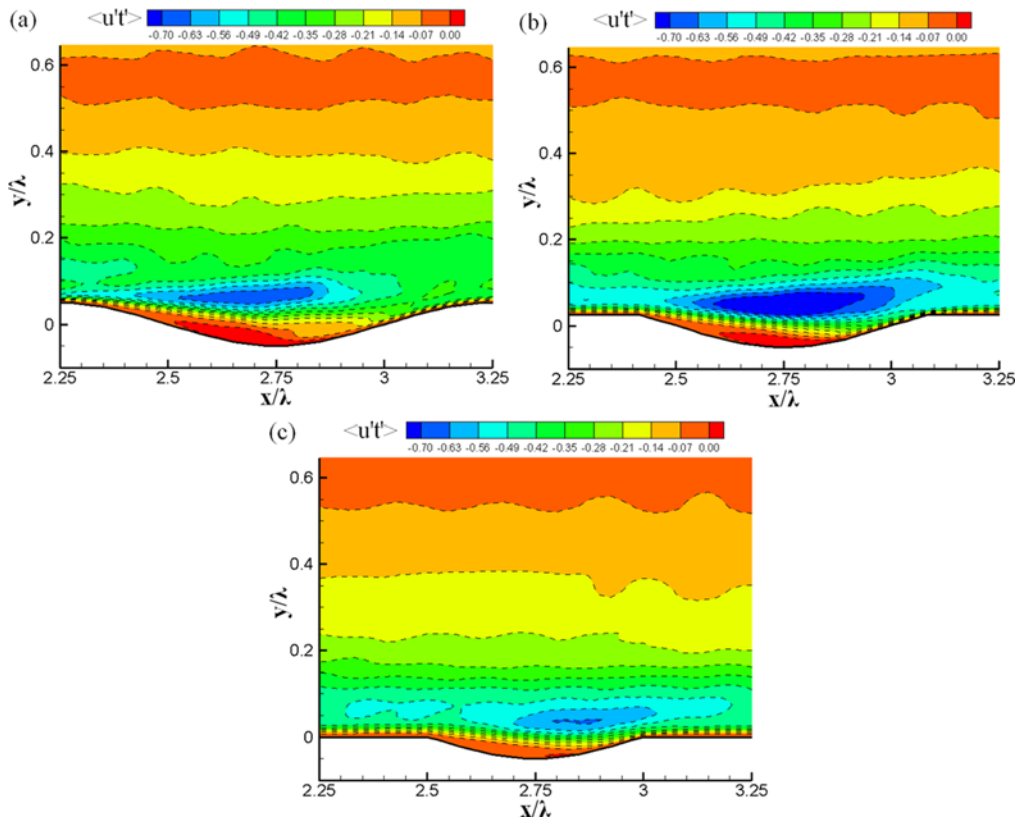

Fig. 13. Contours of the horizontal turbulent heat flux: (a) Case 1, (b) case 2, (c) case 3.

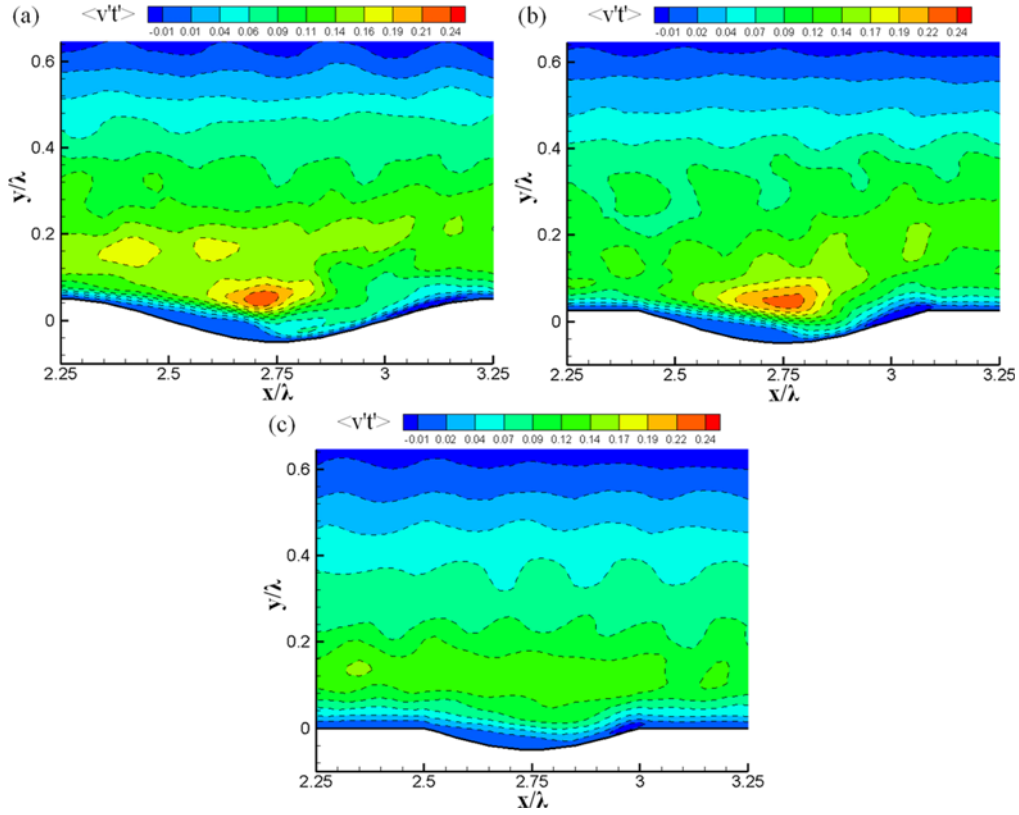

Fig. 14. Contours of the vertical turbulent heat flux: (a) Case 1, (b) case 2, (c) case 3.

to the top wall as shown in Fig. 12, indicating a larger effect of the wall furrow on the vertical fluctuations than it does on the streamwise component. The peaks at points c, d and e are larger than that at points a and b because of the stronger penetration of the core flow at point c and local flow acceleration at points d and e. The magnitude of the wall-normal turbulence intensity increases with the augment of y_h because it is so sensitive to the roughness. It is worth noting that two peak values are located at y/λ=0.0345 and y/λ=0.2, respectively, at point c, in case 1. The first peak is located close to the wall due to the stronger penetration of outer fluids, and the second peak appears far away from the lower wall because of the separated shear layer above separation bubble.

Contours of the horizontal and vertical turbulent heat flux components in the x-y plane with the portions from x/λ=2.25 to 3.25 are shown in Figs. 13 and 14. The heat flux can be defined as the energy in transit due to a temperature difference. The highest turbulent flux is concentrated in the region above the recirculation zones because the separated shear layer in the proximity of the separation region is the locus of large turbulence intensity and the mixing of cool and hot fluids. In case 3, the value of the heat flux near the lower wall is smaller than that in cases 1 and 2, and there is no an obvious highest wall-normal turbulent heat flux value region for weak recirculation. The highest value region of streamwise heat flux moves downward the furrow with the reduction of the recirculation zone size in the cases. The interaction between the recirculation zone and the shear layer principally influences the heat flux. The streamwise turbulent heat flux component above the recirculation zone in case 2 is influenced by the strength of the recirculation flow, temperature and streamwise velocity gradients, which is larger than that in case 1. Although recirculation is the strongest in case 1, the temperature and streamwise velocity gradients above the recirculation zone are small at points b, c and d as shown in Figs. 7 and 10. The intensity of the vertical turbulent heat flux in case 1 is the highest because more smaller scale structures make a significant contribution to the vertical heat flux. The small scale structure is generated on the downslope side of the furrowed wall, accompanied by stronger recirculation flow and the area with highest vertical turbulent heat flux region is enlarged. Based on the results by Kruse et al. [10], it can be predicted that the small scale vortices are contained in the recirculation motion. In other words, a large scale recirculation structure consists of small scale vortices structure.

2-3. Flow Structure and Thermal Performance

A number of ways for the identification of vortices have been proposed, which are powerful in capturing the signatures of a vortex [31]. To reveal the flow structures of present fully turbulent flow, we adopted the second invariant of the velocity gradient tensor, Q-criterion [32], for all cases. Fig. 15 shows the instantaneous vortical structures represented by the isosurfaces of the Q-criterion and colored with values of streamwise vorticity. The streamwise vortices are the dominant structures appearing over the trough and especially developed over the upslope area. As expected, with the increase of y_h, vortices distribute densely and widely near the lower wall due to the early separation and later reattachment, which can be clarified by Figs. 15(a)-(c) corresponding to cases of 1, 2 and 3, respectively. The distribution feature in the present work is similar to the result by Choi et al. [13]. It means that the surface with deeper trough (or larger amplitude) can induce more streamwise vortices. So, it's

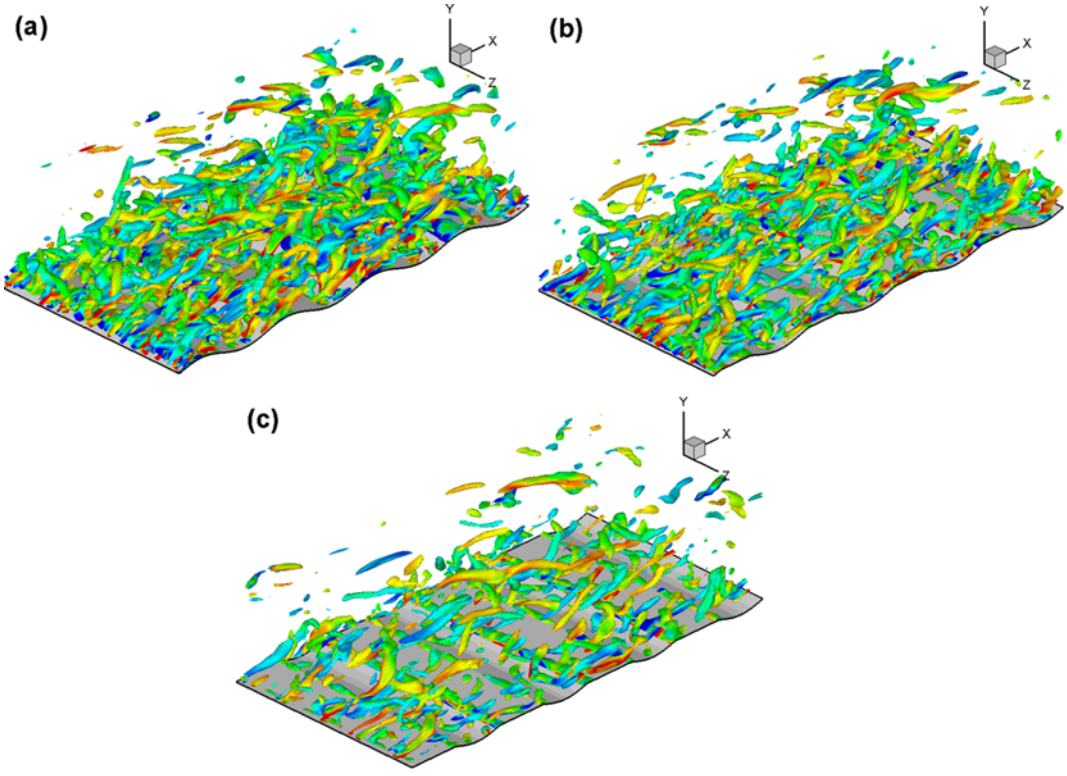

Fig. 15. Isosurfaces distribution of vortical structures at instantaneous time: (a) Case 1, (b) case 2, (c) case 3.

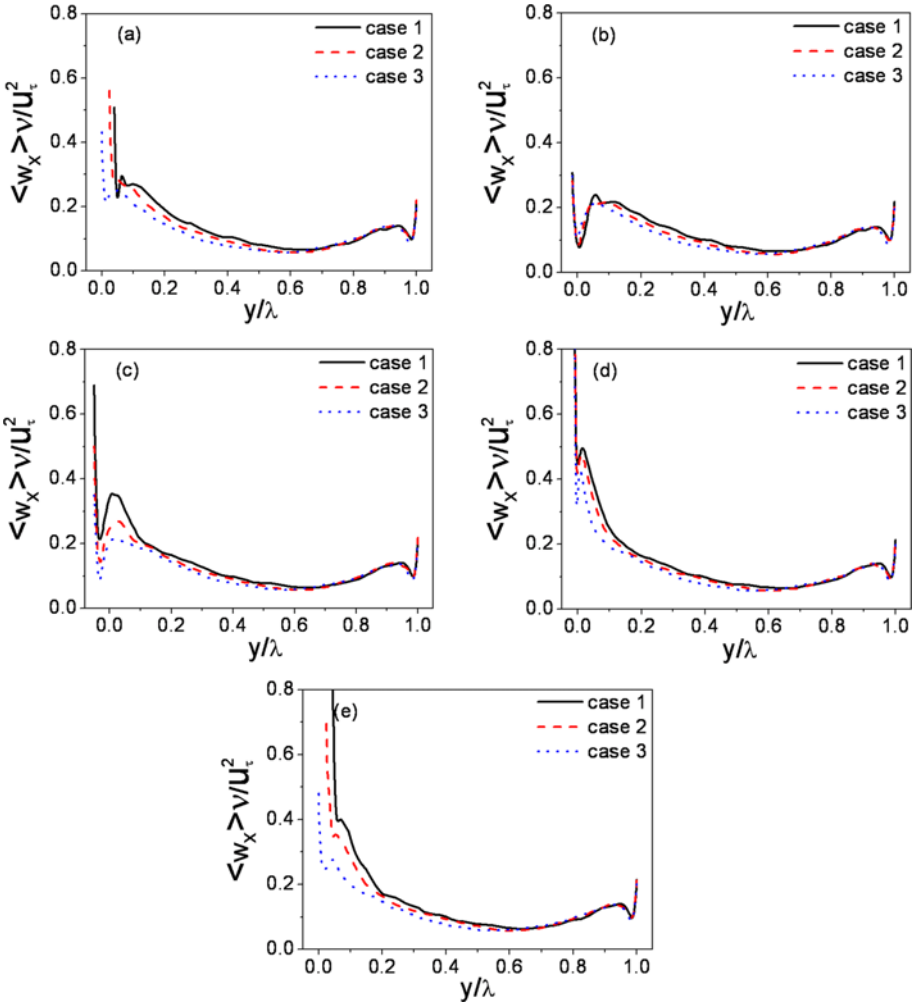

Fig. 16. Streamwise vorticity fluctuations at different streamwise locations: (a) x/λ=2.35, (b) x/λ=2.55, (c) x/λ=2.75, (d) x/λ=2.95, (e) x/λ=3.15.

not difficult to understand the surface with larger amplitude can bring better heat transfer performance.

It can be found that the drastically decreased number of vortices occurs in case 3, and the numbers of the vortices in cases 1 and 2 have no obvious difference. It indicates that the vortices can be induced by wavy wall and the plateau at the wavy wall can weaken the vortices.

The root mean square vorticity fluctuations normalized by the mean shear are presented in Fig. 16. The streamwise vorticity fluctuations decrease rapidly in the vicinity of the lower wall and increase gradually to a maximum, and then decrease again. As expected, the profiles have similar shape, which have a peak in the region close to the upper wall of the channel and show asymmetry due to the furrow effect on the lower wall. The magnitudes of the streamwise vorticity fluctuations in the upslope region are higher than that in the downslope region, which is derived from the vortex stretching, accompanied with the near-wall flow acceleration in the upslope region. The interesting fact is the variation of the peak of the streamwise vorticity fluctuations. The location of the local maximum corresponds to the location of the average streamwise vorticity center. The locations of the streamwise vorticity fluctuations peaks at different streamwise locations are plotted in Fig. 17. It can be found that the locations profile of the average streamwise vorticity center has a similar shape to that of the lower wall. In cases 2 and 3, the profiles shift upward at x/λ=2.55 due to normal velocity caused by the recirculation flow near the separation point, having influence on the sweep motion in front of the separation point. While it does not occurs in case 1 due to powerful sweep motion induced by the increase of the distance from the wave peak to the separation point. Fig. 17(b) presents the distance (d/λ) from the streamwise vorticiy fluctuations peak to the lower wall in all cases. At the plateaus, the streamwise vortices are far away from the wall in case 3. In the trough, the distance in case 2 is larger than that in cases 1 and 3, which has minimum values in case 1. It indicates that the streamwise vortices are far away from the wall in case 2 and spread deep into the trough in case 1. It indicates that the streamwise vortices are bounded in the trough. In the trough, the inflexion points of three cases are shown in Fig. 17(a). Because the streamwise vortices are lifted by the wall curvature when they flow towards the wall, fluid flows toward the wall at a further upstream in case 1 than it does in cases 2 and 3 as a result of stronger recirculation flow in case 1. It also leads to the position distribution of

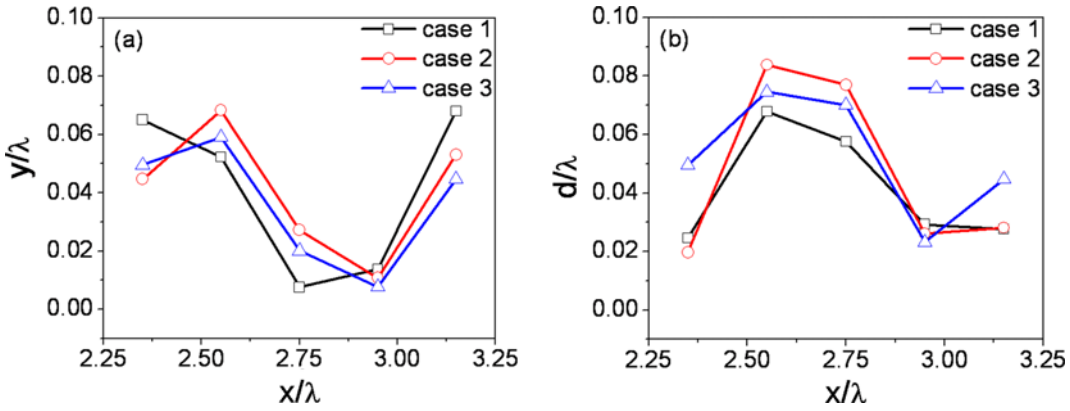

Fig. 17. Locations of the streamwie vortices: (a) Local coordinate, (b) distance from the streamwise vortictiy fluctuations peak to the lower wall.

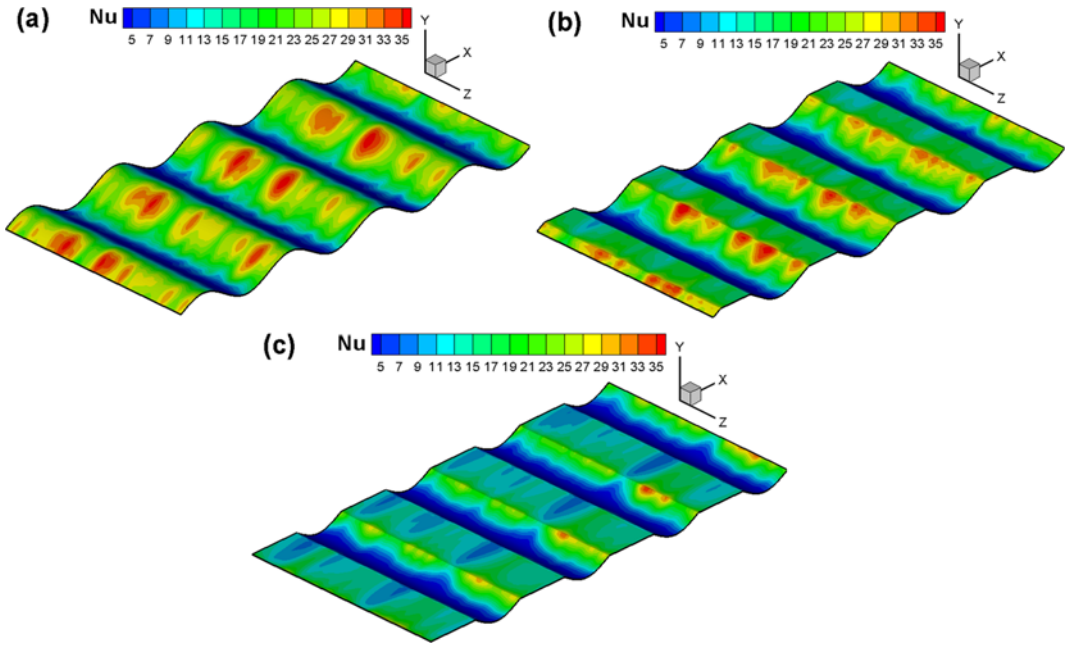

Fig. 18. Nusselt number distributions over lower wall in furrowed channels: (a) Case 1, (b) case 2, (c) case 3.

streamwise vorticity centers at point d as shown in Fig. 17(b).

Fig. 18 illustrates the distribution of the instantaneous Nusselt number at the lower surface. A number of spindle-shaped spots corresponding to high Nusselt numbers are observed in the upslope-region of the lower wall. The spindle-shaped spots are formed by the streamwise vortices generated in the upslope region. Around the near-wall streamwise vortices, down- and up-wash flows exist in both sides of the vortices. At positions beneath the down-wash cold flow, the temperature boundary layer is thickened for being extruded and the Nusselt number is high. The inrush fluids meet very close to the wall and up-wash hot flow is generated between the vortices, and then pushed away from the hot wall, where the temperature boundary layer becomes thick and the Nusselt number remains low. At the plateau in cases 2 and 3, the Nusselt numbers are lower. The reason is that the decrement of the vorticity strength and sparse vorticity distribution. However, the high and low Nusselt number regions are also adjacent as that in up-slope region due to the effect of the streamwise vortices. The Nusselt numbers have lower values at the downslope side of the furrow wall in all cases as a result of the converging of the hot fluids.

Fig. 19 shows the drag coefficients of three cases and the case of a flat surface channel for the sake of comparison. The total drag coefficient (C_T) is composed of the pressure drag coefficient (C_P) and the friction drag coefficient (C_F). The pressure drag coefficient increases rapidly with the increase of y_h. In contrast, the friction drag coefficient shows a decrease behavior with the variation of y_h and is smaller than that of the plane channel due to the blockage effect induced by furrow wall. Because the pressure drag contributes most proportion of total drag, the total mean drag coefficient C_T shows an increment trend. In case 3, C_F is larger than C_P because of smaller recirculation bubble which accelerates the fluid and leads to the increase of the velocity gradient at the wall.

The total drag reduction rate is defined as $R_T=(\overline{C_T}-\overline{C_{T0}})/\overline{C_{T0}}\times 100\%$ where denotes the total mean drag coefficient and $\overline{C_{T0}}$ is the

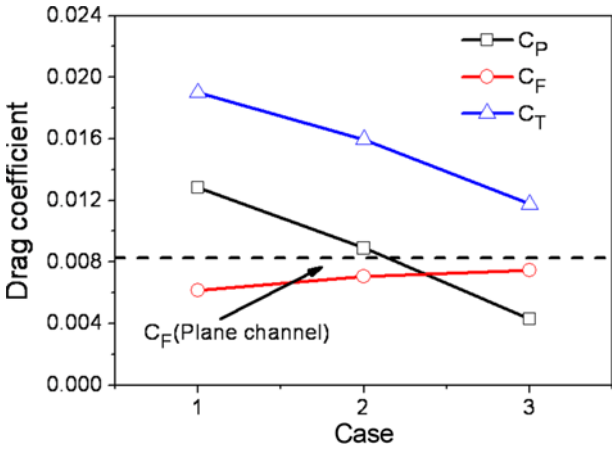

Fig. 19. Drag coefficient as a function of case, where the total drag coefficient is composed of the pressure drag coefficient and the friction drag coefficient.

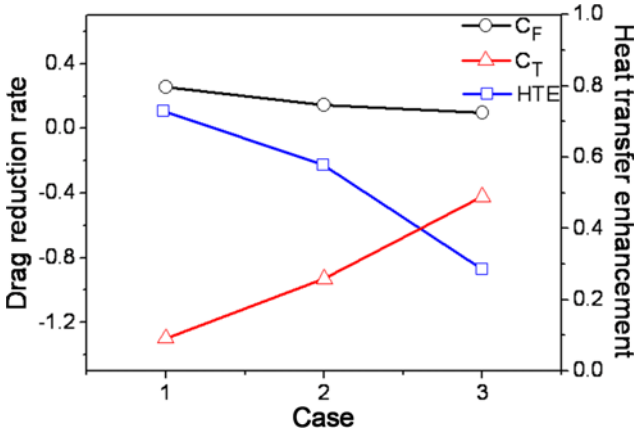

Fig. 20. Drag reduction rate and heat transfer enhancement as a function of case.

total mean drag coefficient of the flat surface. The friction drag reduction rate definition is similar to that of the total drag reduction rate. The heat transfer enhancement rate is expressed as HTE=($\overline{Nu}$−$\overline{Nu_0}$)/$\overline{Nu_0}$×100%, where $\overline{Nu}$ denotes the mean Nusselt number in the three cases and $\overline{Nu_0}$ is the mean Nusselt number of flat surface. The drag reduction and heat transfer enhancement rates are plotted in Fig. 20. In cases 1, 2 and 3, compared with the flat surface, the mean Nusselt number of the furrowed surface increases by about 73%, 58% and 28%, significant reduction in the friction drag coefficient reaches 26%, 15% and 10%, respectively. However, for the decisive effect of the pressure drag, the total drag reduction is −130%, −93% and −42% in cases 1, 2 and 3, respectively. Compared with the result by Elshafei [5], the augment of pressure drag in present is reduced. Especially in case 3, the pressure drag decreases substantially. As shown in Fig. 20, the improvements of heat transfer performance in furrowed channels are also accompanied with an increase in the drag. Therefore, it is important to evaluate the net benefits of using such channels. One method of assessing the relative thermal-hydraulic performance is to synthetically consider the heat transfer and flow features. Thermal performance factor is defined as $\eta=(\overline{Nu}/\overline{Nu_0})/(\overline{C_T}/\overline{C_{T0}})^{1/3}$, where the Nusselt numbers and drag coefficients are referenced by the levels in the channel with flat walls. The thermal performance factor in cases 1, 2 and 3 are 1.31, 1.27 and 1.14, respectively. The present result indicates that the thermal-hydraulic performance is improved when y_h increases. The thermal performance factor in cases 1 and 2 is almost the same. However, in case 2, the drag is much smaller than that in case 1. In the process of heat transfer enhancement, the heat transfer performance depends on the total drag and the pressure drag has decisive influence on the total drag.

CONCLUSIONS

Furrowed surface is a popular passive method extensively used in the heat exchanger. The presence of recirculation cells and streamwise vortices derived from the furrowed surface can break and destabilize the thermal boundary layer and result in enhancing the heat transfer accompanied with drag increment penalty. The present work numerically investigates the flow and heat transfer characteristics in channels with three types of furrowed surface and focuses on their heat transfer enhancement effects, drag coefficients and thermal performance factors. The following conclusions can be obtained:

(1) The size of recirculation zones is enlarged and their centers move upstream with the increase of y_h. It indicates that the recirculation zone is located in the trough of the furrowed surface and can be lifted with the rise of the lower wall. The locations of separation points are more sensitive to roughness than that to the locations of reattachment points. The reason is that the flow separation is derived from the fluctuation of the surface and the reattachment is an addition of the separation. Although the local Nusselt number, friction and pressure coefficients are altered by the appearance of the recirculation zones, their variation presents periodicity and the envelopment trends of Nusselt number and friction coefficient are similar to the shape of furrow surface. It indicates that the surface geometry has critical influence on the features of heat transfer and flow. In addition, the features drop sharply at the front edges of plateaus in cases 2 and 3, which is derived from the flow sudden change caused by the surface fluctuation. Compared with the previous work of wavy surface, the modified wavy surface proposed in the present can strengthen the separation zone in streamwise and lead to the reduction of pressure drag derived from the crest of the wavy surface.

(2) A separated shear layer is located above the recirculation cell. The turbulence intensity is high and mixing of cool and hot fluids occurs in the separated shear layer. The strength of the recirculation cell and the separated shear layer play an important role in the heat flux. The highest heat flux region is located above the separated bubble and moves downstream with the increase of y_h, which implies that the heat transfer can be enhanced by the recirculation derived from the augment of momentum exchange. The recirculation can promote the exchange of momentum and energy among different regions in flow field. For instance, there is not an obvious higher vertical heat flux region due to weaker reversed flow in case 3. In case 2, the horizontal heat flux above the recirculation zone is higher than that in case 1. The reason is that the streamwise velocity and temperature gradients in the shear layer are lower

although the reversed flow is the strongest in case 1.

(3) The streamwise vortices are the dominant flow structures, some of which formed in the rear of the crest (or plateau) and others generated with larger population in the upslope region. The location of streamwise vorticity center in streamwise has a similar shape with the lower surface. However, the locations near the rear edge of the plateau in cases 2 and 3 are slightly lifted as a result of the normal velocity caused by the reversal flow and a shorter distance from the rear edge to the separation point. It's revealed that the reversal flow caused by circulation has an influence on the streamwise vortices. In the trough, the streamwise vortices are further away from the lower wall in case 2 and closest to the lower wall in case 1, inducing inrush of core fluids spreads deep into the trough in case 1. It's found that the deeper trough can gather fluid and bound streamwise vortices.

(4) For the furrow wall surface, the fact that improvement in heat transfer performance is accompanied with a drag increase penalty has been verified by many relevant investigations. The–total drag coefficient of the present furrow surface is higher than that of the flat wall due to the increase of the pressure drag coefficient. However, the friction drag coefficient can be decreased owing to the presence of the low speed fluid accumulation in trough of the furrow surface. The fluid in trough region can suppresses the evolution of streamwise vortices, which is beneficial for drag reduction. But the ledge of the furrow surface can strengthen the disturbance in flow field and lead to the increase of pressure and friction drag. The half-cutting furrowed surface (in case 2) has similar thermal performance factor to sinusoidal wavy wall (in case 1), which is a better choice for heat transfer enhancement when there are demands of lower drag increment penalty. To obtain a better thermal performance factor, it is necessary to combine the trough and ledge portion of the furrow surface properly. On the promise of achieving heat transfer enhancement, keeping the total drag in a relative low level is important for practical engineering application.

ACKNOWLEDGEMENT

The authors gratefully acknowledge the financial support by the National Nature Science Fund of China (No.50476063).

NOMENCLATURE

C_f : skin friction coefficient
C_p : pressure coefficient
c_p : specific heat capacity at constant pressure [$j \cdot kg^{-1} \cdot K^{-1}$]
C_s : Smagorinsky constant
C_T : total drag coefficient
H : full channel height [m]
h : heat transfer coefficient [$w \cdot m^{-2} \cdot k^{-1}$]
$\overline{h_j}$: subgrid scale heat flux
k : thermal conductivity of the fluid [$w \cdot m^{-1} \cdot k^{-1}$]
Nu : Nusselt number
Pr : Prandtl number
q_w : wall heat flux [$w \cdot m^{-2}$]
Re_b : Reynolds number for channel half-height
Re_τ : Reynolds number based on friction velocity
T_{in} : inlet temperature [K]
T_w : bottom wall temperature [K]
T_τ : friction temperature
T^+ : dimensionless temperature normalized by friction temperature
U_b : bulk velocity [$m \cdot s^{-1}$]
U_c : mean centerline velocity [$m \cdot s^{-1}$]
u_τ : friction velocity
u^+ : dimensionless velocity normalized by friction velocity
y_h : the distance from the plane at y=0 to the cutting x-z plane in the wall-normal direction [m]
y_w : profile of the wavy bottom wall [m]
y^+ : dimensionless length normalized by wall variables
α : wave amplitude [m]
δ : channel half-height [m]
Δ : characteristic grid spacing
η : thermal performance factor
θ : nondimensional temperature
λ : wave length [m]
ν : kinematic viscosity [$m^2 \cdot s^{-1}$]
ρ : fluid density [$kg \cdot m^{-3}$]
$\overline{\tau_{ij}}$: subgrid turbulent stress
τ_w : wall shear stress
ω_x : streamwise vorticity

REFERENCES

1. C. Phan, D. L. Holgate and G. J. Griffin, *Korean J. Chem. Eng.*, **20**, 1012 (2003).
2. D. R. Sawyers, M. Sen and H. C. Chang, *Int. J. Heat Mass Transfer*, **41**, 3559 (1998).
3. P. Naphon, *Energ. Convers. Manage.*, **48**, 1516 (2007).
4. S. W. Chang, A. W. Lees and T. C. Chou, *Int. J. Heat Mass Transfer*, **52**, 4592 (2009).
5. E. A. M. Elshafei, M. M. Awad, E. El-Negiry and A. G. Ali, *Energy*, **35**, 101 (2010).
6. J. C. Burns and T. Parks, *J. Fluid Mech.*, **29**, 405 (1967).
7. L. Goldstein and E. M. Sparrow, *J. Heat Trans.-T. ASME*, **99**, 187 (1977).
8. D. P. Zilker, G. W. Cook and T. J. Hanratty, *J. Fluid Mech.*, **82**, 29 (1977).
9. D. P. Zilker and T. J. Hanratty, *J. Fluid Mech.*, **90**, 257 (1979).
10. N. Kruse and P. Rudolf von Rohr, *Int. J. Heat Mass Transfer*, **49**, 3514 (2006).
11. S. Kuhn and P. Rudolf von Rohr, *Int. J. Heat Fluid Flow*, **29**, 94 (2008).
12. C. Maaβ and U. Schumann, *In: Hirschel, E. H. (Ed.), Flow simulation with high performance computers, Notes on Numerical Fluid Mechanics*, **52**, 227 (1996).
13. H. S. Choi and K. Suzuki, *Int. J. Heat Fluid Flow*, **26**, 681 (2005).
14. S. Kuhn, S. Kenjeres and P. Rudolf von Rohr, *Int. J. Therm. Sci.*, **49**, 1209 (2010).
15. C. C. Wang and C. K. Chen, *Int. J. Heat Mass Transfer*, **45**, 2587 (2002).
16. T. S. Park, H. J. Sung and K. Suzuki, *Int. J. Heat Fluid Flow*, **24**, 29 (2003).

17. T. S. Park, H. S. Choi and K. Suzuki, *Int. J. Heat Mass Transfer*, **47**, 2403 (2004).
18. A. Z. Dellil, A. Azzi and B. A. Jubran, *Heat Mass Transfer*, **40**, 793 (2004).
19. H. S. Yoon, O. A. El-Samni, A. T. Huynh, H. H. Chun, H. J. Kim, A. H. Pham and I. P. Park, *Ocean Eng.*, **36**, 697 (2009).
20. P. Naphon, *Int. Commun. Heat Mass*, **36**, 942 (2009).
21. K. A. Hafez, O. A. Elsamni and K. Y. Zakaria, *Alex. Eng. J.*, **50**, 145 (2011).
22. S. Barboy, A. Rashkovan and G. Ziskind, *Int. J. Heat Mass Transfer*, **55**, 3576 (2012).
23. J. Jimenez and P. Moin, *J. Fluid Mech.*, **225**, 213 (1991).
24. J. Kim, P. Moin and R. Moser, *J. Fluid Mech.*, **177**, 133 (1987).
25. D. K. Lilly, *Physics of Fluids*, **4**, 633 (1992).
26. J. W. Deardoff, *J. Fluid Mech.*, **41**, 465 (1970).
27. B. Kader, *Int. J. Heat Mass Transfer*, **43**, 1541 (1981).
28. S. V. Patankar and D. B. Spalding, *Int. J. Heat Mass Transfer*, **15**, 1787 (1972).
29. R. B. Dean, *J. Fluid Eng.*, **100**, 215 (1987).
30. F. P. Incropera and D. P. Dewitt, *Fundam. Heat Mass Transfer*, Wiley, New York (1996).
31. M. S. Chong, A. E. Perry and B. J. Cantwell, *Phys. Fluids A*, **2**, 765 (1990).
32. J. C. R. Hunt, A. A. A. Wray and P. Moin, *Proceedings of the summer program of center for turbulence research*, United States of America (1988).